

Article

Room-Temperature Sputtered Cerium-Doped Indium Oxide Transparent Conducting Electrodes for Bifacial Perovskite Solar Cells: Albedo Utilization and Perovskite/Silicon Tandems

Zachary Ryan Hill Smith¹, Ming-Hsien Li², Chen-Fu Lin³, Farhan Yousuf³,
Keh-Chin Chang^{1,4,*} and Peter Chen^{1,3,5,6,*}¹ International Master's Degree Program on Energy Engineering, National Cheng Kung University, Tainan 701, Taiwan² Department of Electro-Optical Engineering, National Formosa University, Yunlin 63201, Taiwan³ Department of Photonics, National Cheng Kung University, Tainan 701, Taiwan⁴ Department of Aeronautics and Astronautics, National Cheng Kung University, Tainan 701, Taiwan⁵ Hierarchical Green-Energy Materials (Hi-GEM) Research Center, National Cheng Kung University, Tainan 70101, Taiwan⁶ Program on Key Materials, Academy of Innovative Semiconductor and Sustainable Manufacturing, National Cheng Kung University, Tainan 70101, Taiwan* Correspondence: kcchang@mail.ncku.edu.tw (K.-C.C.); petercyc@ncku.edu.tw (P.C.)**How To Cite:** Smith, Z.R.H.; Li, M.-H.; Lin, C.-F.; et al. Room-Temperature Sputtered Cerium-Doped Indium Oxide Transparent Conducting Electrodes for Bifacial Perovskite Solar Cells: Albedo Utilization and Perovskite/Silicon Tandems. *Materials and Sustainability* **2025**, *1*(2), 10. <https://doi.org/10.53941/matsus.2025.100010>.

Received: 26 May 2025

Revised: 25 June 2025

Accepted: 26 June 2025

Published: 30 June 2025

Abstract: Bifacial perovskite solar cells (PSCs) offer the potential for higher power output through tandem configurations with silicon solar cells or by harvesting light from both sides. A high-transmittance and low-resistance transparent electrode is crucial for bifacial PSCs. However, the most widely used transparent conductive oxide (TCO) as transparent electrodes often require energetic ion bombardment during deposition and high post-annealing temperatures to obtain high transmittance and low resistance, making them incompatible for direct deposition onto delicate perovskite films. In this work, a cerium-doped indium oxide (ICO) film, prepared via radio frequency (RF) magnetron sputtering at room temperature (RT), is employed as the top transparent conductive electrode in bifacial PSCs. A 20 nm MoO_x layer is introduced as a buffer layer to protect the underlying spiro-OMeTAD and perovskite layers against sputtering damage. The ICO film, deposited with an RF power of 80 W for 1 h and 20 min at RT, exhibits an amorphous structure with a thickness of 210 nm, a mobility of 8.3 cm²/Vs, a carrier concentration of 6.07 × 10²⁰ cm⁻³, a resistivity of 1.24 × 10⁻³ Ω·cm, and an average transmittance of 89.70% between 550 nm and 1000 nm, resulting in a figure of merit (FOM) of 6.67 × 10⁻³ Ω⁻¹. The fabricated bifacial PSC demonstrates power conversion efficiencies (PCEs) of 15.28% and 10.00% when illuminated from the FTO side and ICO side, respectively. Furthermore, the bifacial PSC under simultaneous illumination from both sides achieves a superior power density compared to the monofacial PSC in albedo utilization. Finally, by mechanically stacking the bifacial PSC as the top cell with a passivated emitter rear contact (PERC) crystalline silicon solar cell as the bottom cell, the 4-terminal perovskite/silicon tandem solar cell achieves a PCE of 21.89%.

Keywords: cerium-doped indium oxide; transparent conducting oxide; magnetron sputtering; perovskite solar cells; bifacial solar cells; 4-terminal tandem solar cells



1. Introduction

Halide-based perovskite materials have been extensively applied in various optoelectronic devices, including solar cells [1–4], light emitting diodes [5], photodetectors [6], X-ray detectors [7,8], and photomemory devices [9], owing to their promising optoelectronic properties such as high absorption efficiency, high carrier mobility, long carrier diffusion length [10,11], tunable bandgap and dimensionality [12–15], low exciton binding energy [16], and high defect tolerance [17]. The power conversion efficiency (PCE) of single-junction perovskite solar cells (PSCs) has reached 27%, while monolithic two-terminal (2T) perovskite/silicon tandem solar cells have already achieved 34.9% [18]. Consequently, employing a tandem configuration of perovskite and silicon solar cells is advantageous for attaining higher power output per unit area [2,19–21].

In perovskite/silicon tandem solar cells, at least one transparent electrode is required for the PSCs [22–24]. Ideal transparent electrode properties include high lateral conductivity to minimize resistive losses and high transmittance across a broad spectrum to improve spectral penetration from visible to near-infrared (NIR) wavelengths [25,26]. Transparent conducting oxides (TCOs) hold great promise as top transparent electrodes for PSCs due to their low sheet resistance, high visible and NIR transmittance, and good chemical stability [27–30]. However, commonly used TCOs like fluorine-doped tin oxide (FTO) and indium tin oxide (ITO) typically require deposition with energetic ions, high doping levels, and post-annealing to achieve high conductivity [31]. High free carrier concentrations resulting from high doping can lead to significant parasitic absorption in the NIR region, thereby reducing the average NIR transmittance [27,32]. Furthermore, the deposition of energetic ions during sputtering and subsequent post-annealing can damage the underlying soft materials in semi-transparent PSCs [33]. Therefore, it is crucial to deposit TCOs with high conductivity but low free carrier absorption to minimize parasitic losses, to implement a buffer layer before TCO deposition to protect underlying layers, and to utilize low sputtering temperatures without post-annealing to prevent degradation of the perovskite active layer and the organic carrier transport layer.

Recently, cerium-doped indium oxide (ICO) has been demonstrated as a promising transparent electrode for silicon heterojunction solar cells [34], bifacial perovskite solar cells [35,36], and perovskite/silicon tandem solar cells [35–37] due to its high conductivity, high transmittance (including high NIR transmittance), and a wide bandgap exceeding 3.5 eV [38,39]. Given that the ionic radius of tetravalent cerium (87 pm) is similar to that of trivalent indium (80 pm), doping with CeO₂ can reduce oxygen vacancies, thereby improving conductivity and NIR transmittance by minimizing free carrier absorption. Furthermore, lattice distortion near the dopant site can be effectively minimized. Notably, ICO can be deposited at room temperature while retaining these desirable properties and mitigating thermal sputtering damage to underlying layers.

Herein, a room-temperature processed ICO film, deposited via RF magnetron sputtering, serves as the top transparent conductive electrode in bifacial PSCs. The device architecture comprises glass/FTO/compact-TiO₂/mesoporous-TiO₂/(FA_{0.81}MA_{0.1}CS_{0.09})Pb(I_{0.9}Br_{0.1})₃ perovskite/spiro-OMeTAD/MoO_x/ICO. By incorporating a 20 nm MoO_x layer as a buffer layer to mitigate sputtering damage, the ICO transparent electrode is successfully deposited onto the delicate spiro-OMeTAD and perovskite layers. The ICO film, optimized with an RF power of 80 W and a deposition time of 4800 s, exhibits an amorphous structure with a thickness of 210 nm, a mobility of 8.3 cm²/Vs, a carrier concentration of 6.07 × 10²⁰ cm⁻³, a resistivity of 1.24 × 10⁻³ Ω·cm, and an average transmittance of 89.70% between 550 nm and 1000 nm, resulting in a FOM of 6.67 × 10⁻³ Ω⁻¹. The fabricated bifacial PSC under AM1.5G solar spectrum irradiation demonstrates a PCE of 15.28% from the FTO side and 10.00% from the ICO side. For PSCs designed for albedo utilization, the additional illumination of the bifacial PSC through the ICO transparent electrode yields a superior power density compared to the monofacial PSC. Furthermore, the 4-terminal (4T) perovskite/silicon tandem solar cell, constructed by mechanically stacking the bifacial PSC with a passivated emitter rear contact (PERC) crystalline silicon solar cell, achieves a PCE of 21.89%.

2. Experimental Section

2.1. Fabrication

First, a fluorine-doped tin oxide (FTO) glass substrate with a sheet resistance of approximately 20 Ω/□ and dimensions of 10 × 10 cm² is used as the substrate. An etching area is then defined using 3 M tape and etched by applying zinc powder and hydrochloric acid (HCl) to the exposed FTO area, followed by rubbing with a cotton swab to remove the reacted FTO and expose the underlying glass. After washing off the residual zinc powder with deionized (DI) water and removing the tape, the substrate is washed with glass cleaner, isopropyl alcohol, and acetone, and then dried using a nitrogen gun. The substrate is placed onto a hot plate and heated to 475 °C for the deposition of the compact TiO₂ (cp-TiO₂) hole blocking layer. This layer is deposited from a TiO₂ precursor solution

with a 1:39 volume ratio of titanium diisopropoxide bis(acetylacetonate) to ethanol, subsequently applied by spray pyrolysis and annealed for 30 min. The mesoporous TiO₂ layer (mp-TiO₂) was prepared by spin-coating diluted TiO₂ paste (1:10 weight ratio in ethanol) at 4000 rpm for 30 s and sintered at 500 °C for 30 min. Triple cation perovskite with the composition (FA_{0.81}MA_{0.1}Cs_{0.09})Pb(I_{0.9}Br_{0.1})₃ at a molar concentration of 1.3 M was then prepared in a nitrogen-filled glove box. Briefly, 0.10056 g of FAI was dissolved in 350 μL of DMF and 150 μL of DMSO. Subsequently, 0.01689 g of CsI was added to the FAI solution and left to dissolve before being added to 0.29965 g of PbI₂ to prepare the CsFAPbI₃ solution. Separately, 0.018195 g of MABr was dissolved in 87.5 μL of DMF and 37.5 μL of DMSO, and then 0.059637 g of PbBr₂ was dissolved in the MABr solution to prepare the MAPbBr₃ solution. Following this, 55.55 μL of the MAPbBr₃ solution was dissolved in the CsFAPbI₃ solution and left to dissolve completely at room temperature. Afterwards, 50 μL of the (FA_{0.81}MA_{0.1}Cs_{0.09})Pb(I_{0.9}Br_{0.1})₃ perovskite solution was deposited onto the substrate, which was spin-coated at 2000 rpm for 10 s, followed by 6000 rpm for 30 s. During the final 15 s of the second spin-coating step, 150 μL of chlorobenzene antisolvent was subsequently dropped onto the wet perovskite film. The as-coated substrate was then annealed on a hot plate at 100 °C for 60 min and subsequently cooled to room temperature. The hole-transporting layer (HTL) was deposited onto the perovskite film via spin coating at 4000 rpm for 30 s. A 50 μL spiro-OMeTAD solution (0.06 M in chlorobenzene) containing two dopants (2.88 μL of TBP and 3.5 μL of 1.8 M lithium bis(trifluoromethylsulfonyl)imide (Li-TFSI) in acetonitrile) was spin-coated onto the perovskite film. Next, the substrate was placed in a vacuum-sealed sputter chamber with a base pressure below 5 × 10⁻⁶ Torr, and approximately 21 nm of molybdenum oxide (MoO_x) was thermally evaporated as a buffer layer to prevent sputtering damage. Subsequently, approximately 200 nm of ICO film was sputter-deposited using RF frequency sputtering.

For the deposition of ICO, an ICO target (97 wt% In₂O₃: 3 wt% CeO₂, 3-inch diameter) was used, and the sputtering chamber was evacuated to a base pressure of 5 × 10⁻⁶ Torr. Subsequently, 30 sccm of pure argon (Ar) gas was introduced into the chamber. Once the chamber pressure reached 5 mTorr, the surface of the ICO target was cleaned for 20 min at 30 W to remove any foreign contaminants. Following this cleaning step, the power was increased at a rate of 1 W/s until the desired working power was reached. The substrate was positioned 10 cm away from the ICO target and moved in a circular motion above the plasma and target, rotating at a speed of 10 rpm during the deposition process. Afterwards, a 60 nm thick gold finger electrode, with a finger spacing of 3.5 mm, was deposited onto the ICO film using thermal evaporation under a vacuum of 5 × 10⁻⁶ Torr. The gold finger electrode allows light to illuminate upon the active area between adjacent fingers and helps reduce the lateral resistance of the ICO film for effective carrier collection.

2.2. Characterizations

Film thickness and sheet resistance of ICO film were examined using alpha step (ET 4000m, Kosaka Instruments, Tokyo, Japan) and four-point probe (KeithLink, New Taipei City, Taiwan), respectively. X-ray diffraction (XRD) profile and transmittance spectra of ICO film were measured using an X-ray diffractometer (D2 Phaser, Bruker, Billerica, MA, USA) and UV-vis spectrometer (U-4100, Hitachi, Tokyo, Japan), respectively. A solar simulator system (SS-F5-3A, Enlitech, Kaohsiung City, Taiwan) was used to measure the characteristic *J-V* curves of the devices under AM1.5G illumination (100 mW/cm²), with a source meter (Keithley 2401, Keithley Instruments, Solon, OH, USA) used to trace the *J-V* data using a scan rate of 2 V/s. The one-sun light intensity (100 mW/cm²) was calibrated using a certified standard silicon solar cell (SRC-2020-KG3, Enlitech). The device's active area of 0.15 cm² was defined by a metal mask, whose transparent region was placed between the adjacent fingers of the gold electrode. For external quantum efficiency (EQE) measurements, a 300 W xenon light, a monochromator (Newport Cornerstone 260, Irvine, CA, USA), and a source meter (Keithley 2401) were integrated.

3. Results and Discussion

3.1. Properties of RF-Sputtered ICO Film

For the fabrication of bifacial PSCs, we employed radio-frequency (RF) sputter deposition to prepare an ICO layer that meets the requirements for high transmittance and good conductivity necessary for photovoltaic applications. While commonly used ITO and FTO require high-temperature fabrication processes to achieve high crystallinity, which can facilitate charge transportation [19,20], depositing the TCO film at elevated temperatures could damage the spiro-OMeTAD hole transport layer (HTL) due to its low glass transition temperature of 116 °C [40]. Figure 1a shows the XRD profiles of RF-sputtered ICO films deposited at room temperature (RT) and 100 °C, using the same RF power of 100 W, working pressure of 5 mTorr, and deposition time of 2400 s. The XRD profile of the ICO film deposited at RT reveals its amorphous nature. In contrast, the ICO film

sputter-deposited at 100 °C exhibits a crystalline structure with a preferred orientation along the (222) facet, consistent with the In₂O₃ cubic bixbyite crystal structure. To prevent the degradation of spiro-OMeTAD during sputtering, the deposition of the ICO film in the PSCs is performed at RT.

Subsequently, we varied the RF power to optimize the transmittance and sheet resistance of the ICO film. With the working pressure fixed at 5 mTorr and the deposition time at 3600 s, and maintaining a room temperature deposition, the transmittance, film thickness, resistance, and figure of merit (FOM) of ICO films deposited at different RF powers are presented in Figure 1b. The FOM of a TCO film serves as a criterion for evaluating its quality by considering both transmittance and resistivity. Haacke's FOM of a TCO film serves as a criterion for evaluating its quality by considering both its transmittance and resistivity, as defined by Equation (1):

$$\Phi_{TC} = \frac{T^{10}}{R_{sheet}} \quad (1)$$

where T is average transmittance, measured by transmittance spectrum, and R_{sheet} is sheet resistance, measured by four-point probe. An ideal TCO film should exhibit high transmittance and low resistivity; however, due to the inverse relationship between thickness and resistivity, a thicker film theoretically possesses lower sheet resistance but compromises transmittance, whereas a very thin film offers high transmittance at the cost of higher sheet resistance. As shown in Figure 1b, the thickness of the ICO film increases with increasing RF power, while the resistance of ICO correspondingly decreases, indicating a higher deposition rate at higher RF powers. Consequently, the FOM of the ICO film improves with increasing RF power from 50 W to 80 W, with the ICO film deposited at 80 W for 3600 s exhibiting the best FOM of $5.4 \times 10^{-3} \Omega^{-1}$. Further increasing the RF power to 90 W results in a higher deposition rate and a thicker ICO film (167 nm) but has a minimal impact on the film resistance, leading to a lower FOM of $4.7 \times 10^{-3} \Omega^{-1}$ for the ICO film. To meet the optical and electronic requirements for the bifacial PSC, we conducted the deposition of the ICO film using an RF power of 80 W and a deposition time of 4800 s, resulting in a film thickness of 210 nm, a resistivity of $1.24 \times 10^{-3} \Omega\text{-cm}$, a mobility of $8.3 \text{ cm}^2/\text{V}$, a carrier concentration of $6.07 \times 10^{20} \text{ cm}^{-3}$, an average transmittance of 89.70% between 550 nm–1000 nm, and a high FOM of $6.61 \times 10^{-3} \Omega^{-1}$.

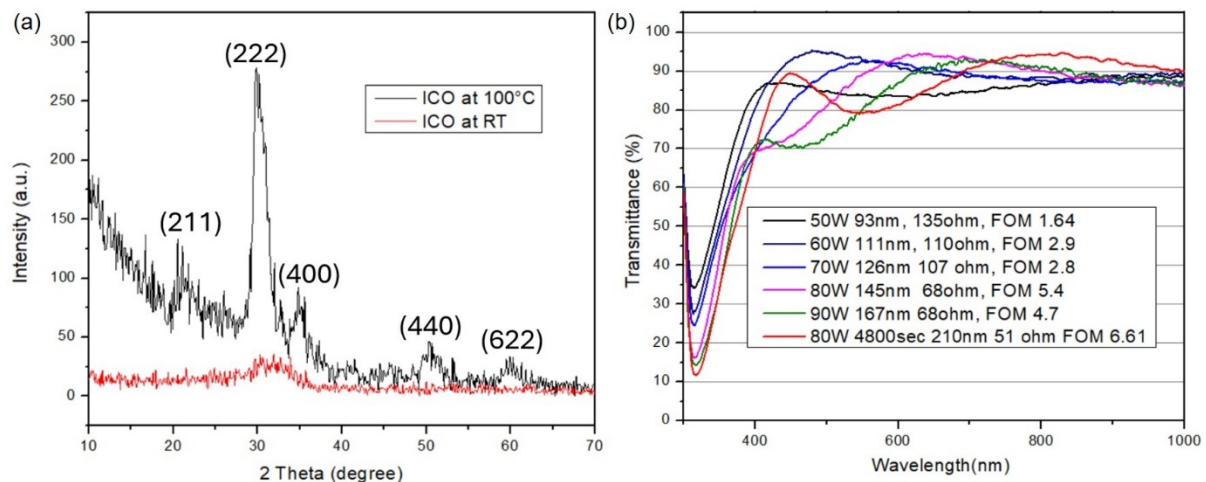


Figure 1. (a) XRD profiles of RF-sputtered ICO film at RT and 100 °C. (b) Transmittance spectra of RF-sputtered ICO film with different RF power.

3.2. Bifacial Perovskite Solar Cells

To mitigate RF sputter damage on the delicate spiro-OMeTAD and perovskite active layer, the introduction of a buffer layer between the hole transport layer (HTL) and the transparent conducting electrode has proven effective [41–43]. Molybdenum oxide (MoO_x) is frequently employed as a buffer layer due to its high resistance to sputter damage and its compatibility with perovskite solar cell manufacturing. MoO_x functions as a protective barrier, shielding the underlying layers from the high-energy bombardment inherent in the sputtering process, which can otherwise cause structural damage and compromise device performance. Furthermore, MoO_x exhibits favorable electronic properties that facilitate the efficient extraction and transport of holes from the HTL to the transparent conducting electrode [30,44].

While the MoO_x layer can withstand sputter bombardment, its thickness is critical to the device's performance. Figure 2a shows the J - V curve of a perovskite solar cell with a n-i-p heterojunction architecture of glass/FTO/compact-TiO₂/mesoporous-TiO₂/MAPbI₃ perovskite/spiro-OMeTAD/MoO_x/Au. A 10 nm MoO_x layer

was deposited via thermal evaporation between the HTL and the top Au electrode. The results indicate that the deposition of 10 nm MoO_x on the spiro-OMeTAD HTL facilitates hole extraction, yielding a PCE of over 15% under reverse scan and a decent external quantum efficiency (EQE) of approximately 85% in the 500–650 nm wavelength range. The corresponding photovoltaic parameters are presented in Table 1. The resulting integrated J_{SC} , obtained by integrating the product of the EQE spectrum and the AM1.5G photon flux, is 20.30 mA/cm², comparable to the J_{SC} value extracted from the J - V curve. Prior to the direct sputtering deposition of the ICO film on the spiro-OMeTAD HTL, a 10 nm MoO_x layer was thermally evaporated onto the spiro-OMeTAD HTL to serve as a buffer layer. The corresponding J - V curve, presented as a non-certified J - V curve in Figure 2a, suggests that a thin 10 nm MoO_x layer is insufficient to withstand the ion bombardment during sputtering.

Consequently, we increased the thickness of the MoO_x layer to approximately 20 nm. When a 20 nm MoO_x buffer layer was thermally evaporated onto the spiro-OMeTAD HTL, the fabricated device, with a device structure of glass/FTO/compact-TiO₂/mesoporous-TiO₂/(FA_{0.81}MA_{0.1}CS_{0.09})Pb(I_{0.9}Br_{0.1})₃ perovskite/spiro-OMeTAD/MoO_x/ICO, illuminated from the FTO side (front side) yielded a certified J - V curve with a decent PCE of 15.28% under reverse scan, potentially due to the 20 nm MoO_x layer facilitating hole extraction and withstanding sputtering bombardment. These results indicate no discernible sputter damage from the RF-sputtered ICO film deposited at a power of 80 W for 4800 s. For the bifacial cell illuminated from the ICO side (rear side), the device exhibited a PCE of 10.00% under reverse scan, resulting in a bifacial factor of 0.65 (defined by the ratio of rear-side illuminated efficiency to front-side illuminated efficiency). Table 1 presents the resultant photovoltaic parameters of the bifacial PSC, which uses a 20 nm MoO_x layer, when illuminated from both the FTO and ICO sides. The EQE spectra of the bifacial cell illuminated from the FTO and ICO sides are shown in Figure 2d. A significant drop in the EQE spectrum for the bifacial cell illuminated from the ICO side between 300 nm and 400 nm is primarily attributed to the parasitic absorption of spiro-OMeTAD. The cutoff wavelength of the EQE spectrum indicates a bandgap of ~1.53 eV for the triple cation perovskite. Figure 2e,f shows photographs of the monofacial and bifacial cells, respectively. In the bifacial cell, a gold finger electrode, with a finger spacing of 3.5 mm, is further thermally evaporated onto the ICO film to enhance charge collection. The energy diagram of the bifacial PSC, illustrated in Figure 2g, shows the separate transport of electron and hole carriers toward the FTO and ICO electrodes. The work function of the ICO film depicted in Figure 2g is referenced from existing literature [35].

3.3. Albedo Effect for the Bifacial Perovskite Solar Cells

Albedo is the reflection and diffusion of light upon incident surfaces which scatter light across the environment. Albedo is measured in a fraction of sun intensity between 0.0–1.0, 0 being no reflected or diffuse radiation and 1 being complete and perfect reflection. Realistically, an albedo of 0 will only be present at night when there is no sunlight and an albedo of near 1.0 is generally only achieved in snow and ice environments due to ground reflection. Albedo is dependent on the ground characteristics, wavelength of the light, along with the time of day and date which can be analyzed by using the Sun's zenith angle. For bifacial illumination applications, bifacial cells are heavily reliant on how much albedo can be absorbed through the rear side of the cell. Bifacial cells are able to boast a higher power output density as a factor of how much albedo light is irradiated from the back side of the cell.

Figure 3a schematically illustrates the effects of albedo on a bifacial solar cell by simultaneously illuminating both sides of the bifacial PSC using two solar light simulators. One solar simulator illuminates the bifacial PSC from the ICO side (rear side) with a varying light intensity from 0.2 to 1 sun (20 mW/cm² to 100 mW/cm²), while the other illuminates the bifacial PSC from the FTO side (front side) with constant light intensities of 20 mW/cm², 60 mW/cm², and 100 mW/cm². These light intensities simulate the working scenarios of solar cells under indoor or rainy (0.2 sun), cloudy (0.6 sun), and clear sky (1 sun) conditions. J - V characterization of the bifacial solar cell under bifacial illumination was then carried out to determine the photovoltaic performance, as shown in Figure 3b–d. As depicted in Figure 3b–d, when the light incident on the bifacial PSC from the FTO side has a constant intensity, the resultant photocurrent of the bifacial PSC illuminated from the ICO side with varying intensity shows a linear increase with the light intensity illuminating the ICO side.

Figure 3e presents the output power density of the bifacial PSC under the aforementioned illumination conditions. A monofacial reference cell was also measured for comparison, and the corresponding power density is summarized in Table 2. For the monofacial cell, increasing the rear-side light intensity does not lead to an increase in the output power density due to the reflection of any additional rear-side light illumination by the metallic rear electrode. Therefore, the monofacial reference cell delivers a constant power density of ~13.59 mW/cm², independent of rear-side light intensity. For the bifacial cell under the same illumination scenario, as the rear-side light intensity illuminated on the bifacial cell gradually increases, the power density increases linearly. Table 2 indicates that the

bifacial cell has the potential to provide a higher power density than the monofacial cell under certain albedo conditions. Under these albedo conditions, it is advantageous to employ a bifacial perovskite cell as opposed to a monofacial perovskite cell. It is often the case that the backside irradiance will be equal to or less than the front side irradiance in everyday use.

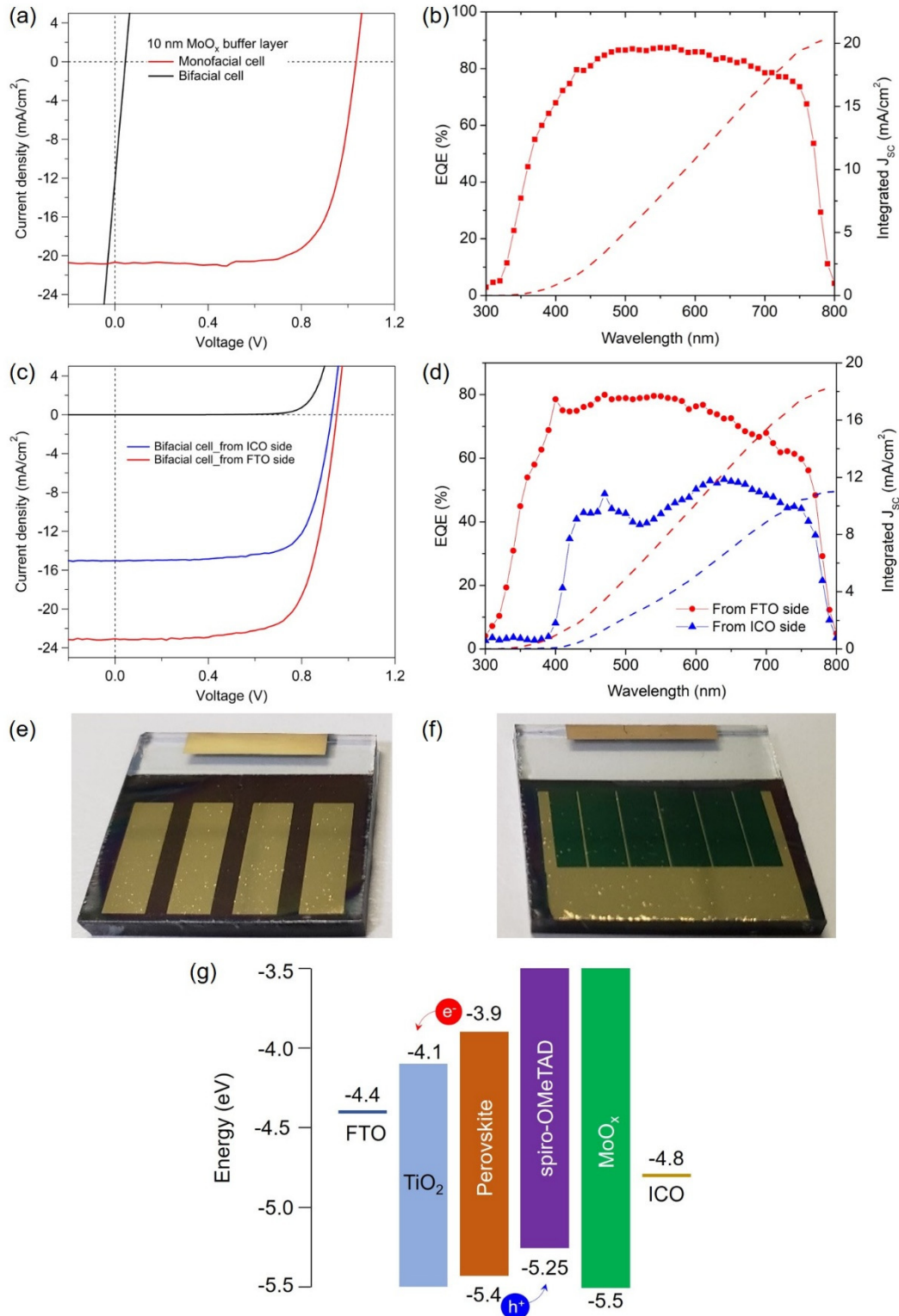


Figure 2. (a) J - V curves and (b) EQE spectra of monofacial and bifacial cells incorporating a 10 nm MoO_x buffer layer. (c) J - V curves and (d) EQE spectra of bifacial cells with a 20 nm MoO_x buffer layer, measured under illumination from the FTO and ICO sides. Photographs of (e) monofacial and (f) bifacial cells. (g) Energy diagram of bifacial cell.

Table 1. Photovoltaic parameters of a monofacial PSC with a 10 nm MoO_x layer and a bifacial PSC with a 20 nm MoO_x layer under AM1.5G illumination (100 mW/cm²) and reverse scan.

| Monofacial Cell (10 nm MoO _x) | V _{oc} (V) | J _{sc} (mA/cm ²) | FF (%) | PCE (%) |
|---|---------------------|---------------------------------------|--------|---------|
| From FTO side | 1.03 | 20.73 | 72.07 | 15.28% |
| Bifacial cell (20 nm MoO _x) | V _{oc} (V) | J _{sc} (mA/cm ²) | FF (%) | PCE (%) |
| From FTO side | 0.95 | 23.11 | 70.00 | 15.28 |
| From ICO side | 0.93 | 15.04 | 72.03 | 10.00 |

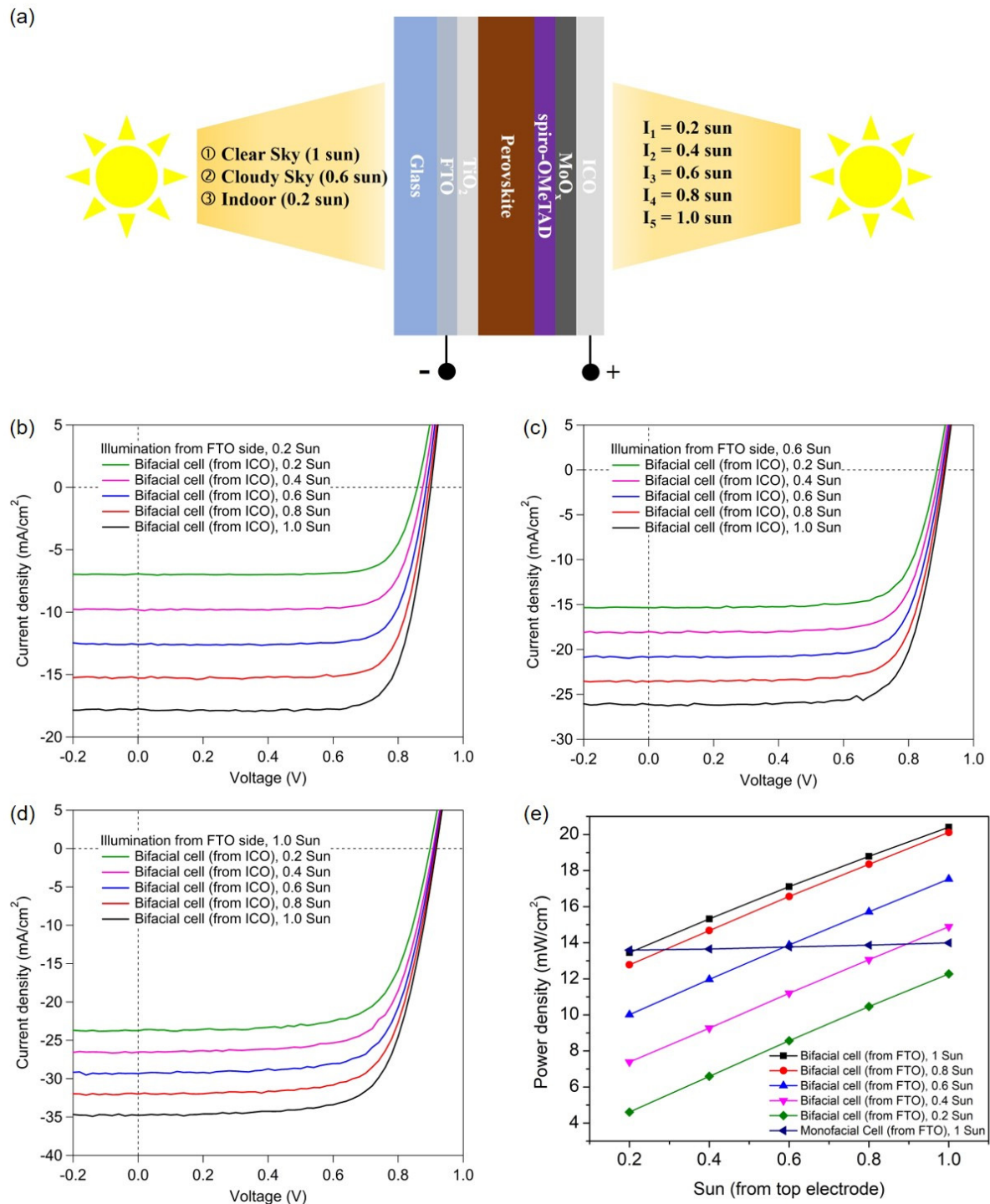


Figure 3. (a) Schematic illustration of a bifacial cell illuminated from both sides, representing simulated light intensity scenarios from the front side as clear sky (1 sun), cloudy sky (0.6 sun), and indoor (0.2 sun). *J-V* curves of the bifacial cell under simultaneous two-sided irradiation with varying light intensities (0.2–1.0 sun) on the ICO side and a constant light intensity of (b) 20 mW/cm², (c) 60 mW/cm², and (d) 100 mW/cm². (e) Power density of the bifacial cell under simultaneous two-sided irradiation with varying light intensities (0.2–1.0 sun) on the ICO side and a constant light intensity of 20 mW/cm², 40 mW/cm², 60 mW/cm², 80 mW/cm², and 100 mW/cm².

Table 2. Power density (mW/cm²) of the bifacial cell under simultaneous two-sided irradiation with varying light intensities (0.2–1.0 sun) on the rear side (ICO electrode for bifacial cell; metal electrode for monofacial cell), while the front side (FTO electrode) maintained a constant light intensity of 0.2, 0.4, 0.6, 0.8, and 1 sun.

| Device | | Monofacial Cell | | Bifacial Cell | | | |
|-----------|------------|-----------------|---------|---------------|---------|---------|---------|
| Rear Side | Front Side | 1.0 sun | 0.2 sun | 0.4 sun | 0.6 sun | 0.8 sun | 1.0 sun |
| | 0.2 sun | | 13.59 | 4.61 | 7.38 | 10.01 | 12.77 |
| 0.4 sun | | 13.65 | 6.59 | 9.26 | 11.97 | 14.67 | 15.32 |
| 0.6 sun | | 13.77 | 8.56 | 11.20 | 13.88 | 16.56 | 17.10 |
| 0.8 sun | | 13.86 | 10.46 | 13.06 | 15.71 | 18.35 | 18.79 |
| 1.0 sun | | 13.99 | 12.27 | 14.89 | 17.53 | 20.12 | 20.40 |

3.4 4-Terminal Perovskite/Silicon Tandem Solar Cells

The ICO thin film is applied in tandem solar cells to enable the transmission of the NIR wavelength range (unabsorbed by the wide bandgap active perovskite material with a bandgap of 1.5–1.7 eV) through the device for more efficient absorption by the bottom silicon cell with a narrower bandgap of 1.12 eV. For the fabrication of a 4T tandem cell, a PERC crystalline silicon solar cell was selected as the bottom cell. Figure 4a,b illustrate the *J-V* curves and EQE spectra of the bifacial PSC, PERC-Si cell, and PERC-Si cell filtered by the bifacial PSC, respectively, alongside the photovoltaic parameters summarized in Table 3. The unfiltered PERC-Si cell achieves a PCE of 18.88% with an average EQE of 89.55% within the 400–1000 nm wavelength range. In the mechanical perovskite/silicon (Si) tandem solar cell, the as-fabricated bifacial PSC with an ICO transparent electrode was subsequently used as the top cell and placed on the PERC-Si cell. The transmittance spectrum of the bifacial PSC, shown in Figure 4b, reveals an average visible-light transmittance (AVT) of ~6.78%. The equation for estimating AVT is provided in Equation (2) [45].

$$AVT (\%) = \frac{\int_{400}^{800} T(\lambda) d\lambda}{(800-400)} \quad (2)$$

where λ is the wavelength and $T(\lambda)$ is the transmittance at λ . As demonstrated by the EQE spectra in Figure 4b, the bifacial PSC effectively absorbs the UV-Vis light range between 300 and 810 nm, which aligns well with its low AVT. The PERC-Si cell, when filtered by the bifacial PSC under AM1.5G 1-sun illumination, exhibits a PCE of 6.61%. Ultimately, the 4T perovskite/Si tandem cell yields a total PCE of 21.89%. Notably, the PERC-Si cell, filtered by the bifacial PSC, exhibits an EQE response primarily within the 800–1000 nm range, as depicted in Figure 4b. Furthermore, the EQE profile of the filtered PERC-Si cell closely follows the transmittance profile of the bifacial PSC. This indicates that the EQE response of filtered PERC-Si cell is limited by the NIR transmittance of the bifacial PSC.

This drop in NIR EQE is primarily attributed to the optical loss by the perovskite top cell stack, particularly the NIR absorption by the FTO glass substrate and ICO film, refractive index mismatch induced reflection between adjacent layers, and light scattering from uneven surfaces, especially from the mp-TiO₂ layer. In addition, reflection losses at the glass interface of a mechanically airgap stacked tandem, such as the perovskite/ICO and ICO/Si boundaries can prevent a significant portion of photons from the NIR region to reach the silicon cell [46]. Filtering losses due to the spectral transmission profile of the perovskite top cell also play a role, as the top-cell structure may partially absorb or scatter photons intended for the bottom cell [47].

To improve NIR response and mitigate these losses, it is important to optimize the optical properties of the TCO to account for a tandem design, tuning the deposition parameters to maximize NIR transmission, as well as using a perovskite stack structure designed with bifaciality in mind. Additionally, employing advanced light management techniques, including textured surfaces or nanostructured interfaces, can minimize reflection and enhance light trapping across the tandem [26]. Moreover, tuning the perovskite bandgap to a slightly wider value (e.g., ~1.7–1.8 eV) allows more NIR photons to pass through to the silicon bottom cell without significant compromise to the top-cell photocurrent [48,49]. Finally, one could incorporate anti-reflective coatings or optical spacers designed for broad-spectrum performance, further increasing the photon transmission in the NIR region. These techniques could be utilized in future research to improve NIR transmission to the bottom cell and enhance overall tandem efficiency.

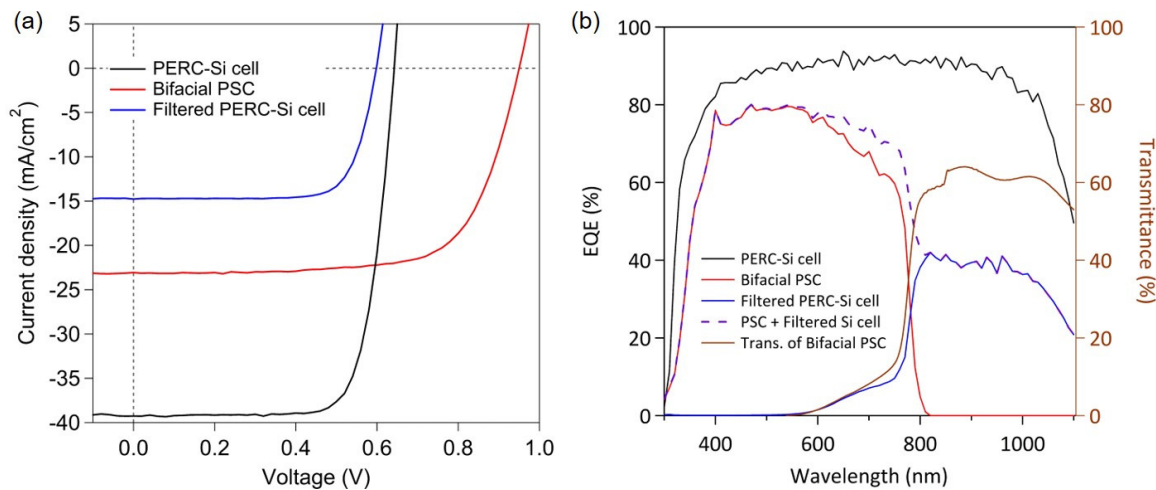


Figure 4. (a) J - V curves and (b) EQE spectra of bifacial PSC, PERC-Si cell, and filtered PERC-Si cell by bifacial PSC, and transmittance spectrum of bifacial PSC.

Table 3. Photovoltaic parameters of bifacial PSC, PERC-Si cell, and filtered PERC-Si cell by bifacial PSC under AM1.5G illumination (100 mW/cm²).

| Device | V_{oc} (V) | J_{sc} (mA/cm ²) | FF (%) | PCE (%) |
|---|--------------|--------------------------------|--------|---------|
| PERC-Si cell | 0.64 | 39.27 | 75.12 | 18.88 |
| Bifacial PSC (illuminated from FTO side) | 0.95 | 23.11 | 70.00 | 15.28 |
| Filtered PERC-Si cell | 0.60 | 14.72 | 75.47 | 6.61 |
| 4T perovskite/Si tandem cell (Calculated) | \ | \ | \ | 21.89 |

4. Conclusions

In summary, a room-temperature RF-sputtered ICO film is applied in a bifacial PSC with an n-i-p device structure. A 20 nm MoO_x layer, capable of protecting the underlying spiro-OMeTAD and perovskite layers against sputtering damage caused by RF sputtering, functions as a buffer layer. The as-deposited ICO film exhibits a resistivity of $1.24 \times 10^{-3} \Omega \cdot \text{cm}$ and an average transparency of 89.70% between 550 nm and 1000 nm, resulting in a FOM of $6.67 \times 10^{-3} \Omega^{-1}$. The application of bifacial PSCs in albedo utilization and tandem solar cells is further demonstrated. In albedo utilization, the bifacial PSC under simultaneous illumination from both sides shows its potential to achieve a higher power density than the monofacial PSC. Moreover, the bifacial PSC achieves PCEs of 15.28% and 10.00% under illumination from the FTO and ICO sides, respectively. Ultimately, the 4T perovskite/silicon tandem solar cell delivers a PCE of 21.89%.

Author Contributions

Z.R.H.S.: Methodology, Validation, Formal analysis, Investigation, Data Curation, and Visualization. M.-H.L.: Visualization, Interpretation of data, Writing—Original Draft, and Writing—Review & Editing. C.-F.L.: Interpretation of data, and Writing—Review & Editing. F.Y.: Validation. K.-C.C.: Resources, Supervision. P.C.: Conceptualization, Methodology, Writing—Review & Editing, Supervision, Project administration, and Funding acquisition. All authors have read and agreed to the published version of the manuscript.

Funding

The authors are grateful to the research grant from the Ministry of Science and Technology, National Science and Technology Council of Taiwan (MOST 110-2221-E-006-200, MOST 111-2221-E-006-061-MY2, NSTC 113-2223-E-006-011). This work was financially supported by the Hierarchical Green-Energy Materials (Hi-GEM) Research Center, from The Featured Areas Research Center Program within the framework of the Higher Education Sprout Project by the Ministry of Education (MOE) in Taiwan. This research was supported in part by Higher Education Sprout Project, Ministry of Education to the Headquarter of University Advancement at National Cheng Kung University (NCKU). The authors gratefully acknowledge the use of EM003600 of MOST 106-2731-M-006-001 equipment belonging to the Core Facility Center of National Cheng Kung University.

Data Availability Statement

The datasets generated during and/or analyzed during the current study are available from the corresponding author upon reasonable request.

Conflicts of Interest

All authors declare no financial or non-financial conflict of interest.

References

1. Afroz, M.; Ratnesh, R.K.; Srivastava, S.; et al. Perovskite solar cells: Progress, challenges, and future avenues to clean energy. *Sol. Energy* **2025**, *287*, 113205. <https://doi.org/10.1016/j.solener.2024.113205>.
2. Mei, J.; Yan, F. Recent Advances in Wide-Bandgap Perovskite Solar Cells. *Adv. Mater.* **2025**, 2418622. <https://doi.org/10.1002/adma.202418622>.
3. Tang, G.; Chen, L.; Cao, X.; et al. A Review on Recent Advances in Flexible Perovskite Solar Cells. *Sol. RRL* **2025**, *9*, 2400844. <https://doi.org/10.1002/solr.202400844>.
4. Wallach, T.; Etgar, L. Highly transparent and semi-transparent perovskites and their applications. *Appl. Phys. Rev.* **2025**, *12*, 011314. <https://doi.org/10.1063/5.0237977>.
5. Liu, Y.; Ma, Z.; Zhang, J.; et al. Light-Emitting Diodes Based on Metal Halide Perovskite and Perovskite Related Nanocrystals. *Adv. Mater.* **2025**, 2415606. <https://doi.org/10.1002/adma.202415606>.
6. Li, X.; Aftab, S.; Mukhtar, M.; et al. Exploring Nanoscale Perovskite Materials for Next-Generation Photodetectors: A Comprehensive Review and Future Directions. *Nano Micro Lett.* **2024**, *17*, 28. <https://doi.org/10.1007/s40820-024-01501-6>.
7. Li, F. Halide perovskites, a game changer for future medical imaging technology. *Biophys. Rev.* **2025**, *6*, 011302. <https://doi.org/10.1063/5.0217068>.
8. Yao, F.; Dong, K.; Ke, W.; et al. Micro/Nano Perovskite Materials for Advanced X-ray Detection and Imaging. *ACS Nano* **2024**, *18*, 6095–6110. <https://doi.org/10.1021/acsnano.3c10116>.
9. Feng, Z.; Wang, J.; Chen, F.; et al. Coupling Light into Memristors: Advances in Halide Perovskite Resistive Switching and Neuromorphic Computing. *Small Methods* **2025**, 2500089. <https://doi.org/10.1002/smt.202500089>.
10. Bagade, S.S.; Patel, P.K. A comprehensive review on potential of diffusion length enhancement to upraise perovskite solar cell performance. *Phys. Scr.* **2024**, *99*, 052003. <https://doi.org/10.1088/1402-4896/ad3a26>.
11. Zhang, M.; Wu, C.; Yin, M.; et al. High Efficiency Tin Halide Perovskite Solar Cells with over 1 Micrometer Carrier Diffusion Length. *Adv. Funct. Mater.* **2024**, *34*, 2410772. <https://doi.org/10.1002/adfm.202410772>.
12. Miah, M.H.; Khandaker, M.U.; Rahman, M.B.; et al. Band gap tuning of perovskite solar cells for enhancing the efficiency and stability: Issues and prospects. *RSC Adv.* **2024**, *14*, 15876–15906. <https://doi.org/10.1039/D4RA01640H>.
13. Novikov, S.A.; Valueva, A.D.; Klepov, V.V. Band gap engineering and photoluminescence tuning in halide double perovskites. *Dalton Trans.* **2024**, *53*, 12442–12449. <https://doi.org/10.1039/D4DT01420K>.
14. Li, X.; Aftab, S.; Hussain, S.; et al. Dimensional diversity (0D, 1D, 2D, and 3D) in perovskite solar cells: Exploring the potential of mixed-dimensional integrations. *J. Mater. Chem. A* **2024**, *12*, 4421–4440. <https://doi.org/10.1039/D3TA06953B>.
15. Zhang, Q.; Zhang, D.; Cao, B.; et al. Improving the Operational Lifetime of Metal-Halide Perovskite Light-Emitting Diodes with Dimension Control and Ligand Engineering. *ACS Nano* **2024**, *18*, 8557–8570. <https://doi.org/10.1021/acsnano.3c13136>.
16. Muhammad, Z.; Rashid, A. Exciton binding energies and polaron interplay in the optically excited state of organic–inorganic lead halide perovskites. *Mater. Adv.* **2025**, *6*, 13–38. <https://doi.org/10.1039/D4MA00454J>.
17. Liu, G.; Ghasemi, M.; Wei, Q.; et al. Dynamic Defect Tolerance in Metal Halide Perovskites: From Phenomena to Mechanism. *Adv. Energy Mater.* **2025**, *15*, 2405239. <https://doi.org/10.1002/aenm.202405239>.
18. Available online: <https://www2.nrel.gov/pv/cell-efficiency> (accessed on 18 May 2025).
19. Yang, X.; Zhu, Y.; Yan, S.; et al. Blade-Coating Perovskites for Tandem Devices: Liquid Mechanism, Film Formation, and Performance. *Sol. RRL* **2025**, *9*, 202500149. <https://doi.org/10.1002/solr.202500149>.
20. Wang, H.; Lin, W.; Wang, Y.; et al. Perovskite/silicon tandem solar cells: A comprehensive review of recent strategies and progress. *Semicond. Sci. Technol.* **2025**, *40*, 023001. <https://doi.org/10.1088/1361-6641/adab11>.
21. Adnan, M.; Irshad, Z.; Lim, J. Impact of structural advancements interface engineering operational stability and commercial viability of perovskite/silicon tandem solar cells. *Sol. Energy* **2025**, *286*, 113190. <https://doi.org/10.1016/j.solener.2024.113190>.
22. Guo, H.; Hou, F.; Ren, X.; et al. Recent Progresses on Transparent Electrodes and Active Layers Toward Neutral, Color Semitransparent Perovskite Solar Cells. *Sol. RRL* **2023**, *7*, 2300333. <https://doi.org/10.1002/solr.202300333>.
23. Hou, F.; Ren, X.; Guo, H.; et al. Monolithic perovskite/silicon tandem solar cells: A review of the present status and solutions toward commercial application. *Nano Energy* **2024**, *124*, 109476. <https://doi.org/10.1016/j.nanoen.2024.109476>.
24. Kumar, P.; Shankar, G.; Pradhan, B. Recent progress in bifacial perovskite solar cells. *Appl. Phys. A* **2022**, *129*, 63. <https://doi.org/10.1007/s00339-022-06337-8>.

25. Jung, H.; Kim, G.; Jang, G.S.; et al. Transparent Electrodes with Enhanced Infrared Transmittance for Semitransparent and Four-Terminal Tandem Perovskite Solar Cells. *ACS Appl. Mater. Interfaces* **2021**, *13*, 30497–30503. <https://doi.org/10.1021/acsami.1c02824>.
26. Feng, Y.; Kim, P.; Nemitz, C.A.; et al. Boosting charge collection efficiency via large-area free-standing Ag/ZnO core-shell nanowire array electrodes. *Prog. Nat. Sci. Mater. Int.* **2019**, *29*, 124–128. <https://doi.org/10.1016/j.pnsc.2019.03.002>.
27. Chavan, G.T.; Kim, Y.; Khokhar, M.Q.; et al. A Brief Review of Transparent Conducting Oxides (TCO): The Influence of Different Deposition Techniques on the Efficiency of Solar Cells. *Nanomaterials* **2023**, *13*, 1226.
28. Principe, J.; Duarte, V.C.M.; Mendes, A.; et al. Influence of the Transparent Conductive Oxide Type on the Performance of Inverted Perovskite Solar Cells. *ACS Appl. Energy Mater.* **2023**, *6*, 12442–12451. <https://doi.org/10.1021/acsam.3c02292>.
29. Chen, Y.-J.; Li, M.-H.; Huang, J.-C.-A.; et al. The Cu/Cu₂O nanocomposite as a p-type transparent-conductive-oxide for efficient bifacial-illuminated perovskite solar cells. *J. Mater. Chem. C* **2018**, *6*, 6280–6286. <https://doi.org/10.1039/C8TC00768C>.
30. Chiang, Y.-H.; Peng, C.-C.; Chen, Y.-H.; et al. The utilization of IZO transparent conductive oxide for tandem and substrate type perovskite solar cells. *J. Phys. D Appl. Phys.* **2018**, *51*, 424002. <https://doi.org/10.1088/1361-6463/aad71c>.
31. Li, P.; Li, F.; Ma, J.; et al. Over 500 °C stable transparent conductive oxide for optoelectronics. *InfoMat* **2024**, *6*, e12607. <https://doi.org/10.1002/inf2.12607>.
32. Abe, Y.; Nishimura, T.; Yamada, A. Optimum Electrical and Optical Properties of Transparent Conducting Oxide for Cu(In,Ga)Se₂ Photovoltaic Module Applications. *Phys. Status Solidi* **2024**, *221*, 2300641. <https://doi.org/10.1002/pssa.202300641>.
33. Yang, Q.; Duan, W.; Eberst, A.; et al. Origin of sputter damage during transparent conductive oxide deposition for semitransparent perovskite solar cells. *J. Mater. Chem. A* **2024**, *12*, 14816–14827. <https://doi.org/10.1039/D3TA06654A>.
34. Özkol, E.; Magalhães, M.M.R.; Zhao, Y.; et al. Optimization and integration of room temperature RF sputtered ICO as TCO layers in high-performance SHJ solar cells. *Sol. Energy Mater. Sol. Cells* **2025**, *288*, 113637. <https://doi.org/10.1016/j.solmat.2025.113637>.
35. Zhang, L.; Che, Z.; Shang, J.; et al. Cerium-Doped Indium Oxide as a Top Electrode of Semitransparent Perovskite Solar Cells. *ACS Appl. Mater. Interfaces* **2023**, *15*, 10838–10846. <https://doi.org/10.1021/acsami.2c22942>.
36. An, S.; Chen, P.; Hou, F.; et al. Cerium-doped indium oxide transparent electrode for semi-transparent perovskite and perovskite/silicon tandem solar cells. *Sol. Energy* **2020**, *196*, 409–418. <https://doi.org/10.1016/j.solener.2019.12.040>.
37. Lee, P.-H.; Wu, T.-T.; Li, C.-F.; et al. Featuring Semitransparent p–i–n Perovskite Solar Cells for High-Efficiency Four-Terminal/Silicon Tandem Solar Cells. *Sol. RRL* **2022**, *6*, 2100891. <https://doi.org/10.1002/solr.202100891>.
38. Zhang, Y.; Gan, Y.; Gan, T.; et al. High mobility cerium-doped indium oxide thin films prepared by reactive plasma deposition without oxygen. *Vacuum* **2022**, *206*, 111512. <https://doi.org/10.1016/j.vacuum.2022.111512>.
39. Wan, S.; Man, X.; Zhang, P.; et al. Ultra-Transparent Cerium-Doped Indium Oxide Films Deposited with Industry-Scale Reactive Plasma Deposition. *J. Electron. Mater.* **2024**, *53*, 4829–4840. <https://doi.org/10.1007/s11664-024-11198-3>.
40. Tumen-Ulzii, G.; Qin, C.; Matsushima, T.; et al. Understanding the Degradation of Spiro-OMeTAD-Based Perovskite Solar Cells at High Temperature. *Solar RRL* **2020**, *4*, 2000305. <https://doi.org/10.1002/solr.202000305>.
41. Magliano, E.; Mariani, P.; Agresti, A.; et al. Semitransparent Perovskite Solar Cells with Ultrathin Protective Buffer Layers. *ACS Appl. Energy Mater.* **2023**, *6*, 10340–10353. <https://doi.org/10.1021/acsam.3c00735>.
42. Mujahid, M.; Chen, C.; Zhang, J.; et al. Recent advances in semitransparent perovskite solar cells. *InfoMat* **2021**, *3*, 101–124. <https://doi.org/10.1002/inf2.12154>.
43. Lou, J.; Feng, J.; Cao, Y.; et al. Designed multi-layer buffer for high-performance semitransparent wide-bandgap perovskite solar cells. *Mater. Adv.* **2023**, *4*, 1777–1784. <https://doi.org/10.1039/D2MA01089E>.
44. Liang, F.; Ying, Z.; Lin, Y.; et al. High-Performance Semitransparent and Bifacial Perovskite Solar Cells with MoO_x/Ag/WO_x as the Rear Transparent Electrode. *Adv. Mater. Interfaces* **2020**, *7*, 2000591. <https://doi.org/10.1002/admi.202000591>.
45. Shi, H.; Zhang, L.; Huang, H.; et al. Simultaneous Interfacial Modification and Defect Passivation for Wide-Bandgap Semitransparent Perovskite Solar Cells with 14.4% Power Conversion Efficiency and 38% Average Visible Transmittance. *Small* **2022**, *18*, 2202144. <https://doi.org/10.1002/sml.202202144>.
46. Sahli, F.; Werner, J.; Kamino, B.A.; et al. Fully textured monolithic perovskite/silicon tandem solar cells with 25.2% power conversion efficiency. *Nat. Mater.* **2018**, *17*, 820–826. <https://doi.org/10.1038/s41563-018-0115-4>.
47. Werner, J.; Weng, C.-H.; Walter, A.; et al. Efficient Monolithic Perovskite/Silicon Tandem Solar Cell with Cell Area > 1 cm². *J. Phys. Chem. Lett.* **2016**, *7*, 161–166. <https://doi.org/10.1021/acs.jpcclett.5b02686>.
48. Hörantner, M.T.; Snaith, H.J. Predicting and optimising the energy yield of perovskite-on-silicon tandem solar cells under real world conditions. *Energy Environ. Sci.* **2017**, *10*, 1983–1993. <https://doi.org/10.1039/C7EE01232B>.
49. Huang, Y.-C.; Huang, S.-W.; Li, C.-F.; et al. A comprehensive optimization of highly efficient MA-Free wide-bandgap perovskites for 4-T Perovskite/Silicon tandem solar cells. *Chem. Eng. J.* **2025**, *503*, 158272. <https://doi.org/10.1016/j.cej.2024.158272>.